Electron paramagnetic resonance investigations of MgSiF$_6$.6H$_2$O:Mn^{2+} single crystals

Electron paramagnetic resonance investigations of MgSiF$_6$ · 6H$_2$O:Mn^{2+} single crystals

A Kassiba†, R Hrabański‡, D Bonhomme† and A Hader†

† Equipe de Physique de l'État Condensé (Unité de Recherche associé au CNRS) Université du Maine, avenue Olivier Messiaen, 72017 Le Mans Cédex, France
‡ Institute of Physics, Technical University of Czestochowa, Al. Armii Krajowej 19, 42-200 Czestochowa, Poland

Abstract. EPR studies were performed on MgSiF$_6$ · 6H$_2$O single crystals using Mn^{2+} paramagnetic probes substituted for Mg^{2+} ions. The spin-Hamiltonian parameters (SHPs) are determined accurately for the different phases: the monoclinic phase below $T_c = 301$ K, the rhombohedral phase above $T_0 = 370$ K and the intermediate phase between T_c and T_0. The sets of SHPs are interpreted in the light of structural changes between these phases. The EPR line features in the intermediate phase are analysed in the framework of a static and an order–disorder model. We interpret the EPR spectrum behaviours around $T_0 - 20$ K as the occurrence of a crossover between static and dynamic disorder in the material.

1. Introduction

The ABF$_6$ · 6H$_2$O materials (A ≡ Mg, or Fe; B ≡ Si, Ge, Ti, etc) have attracted much attention because of their structural phase transitions with some unusual aspects [1]. In particular, in magnesium fluorosilicate, a phase transition occurs at around 298 K between a low-temperature monoclinic phase ($P2_1/c$) and a domain-like phase with the overall space group $P\bar{3}$ [2]. Previously, Hrabański *et al* [3] have reported phase transition effects in the EPR spectrum of Mn^{2+} in this system.

Recently, Ziatdinov *et al* [4] and Hrabański [5], using the EPR technique, concluded that an intermediate incommensurate-like structure exists in the system between 298 and 370 K. Their EPR spectra were analysed in the framework of an incommensurate distribution of resonance lines [6].

In this paper, we report EPR measurements above $T_0 = 370$ K and below $T_c = 301$ K in order to determine accurately the Mn^{2+} spin-Hamiltonian parameters (SHPs) in both phases. The aim is to identify and interpret the SHPs which appear below T_c because of the symmetry breaking. The idea of this approach is to see whether knowledge of the EPR parameters in the low- and high-temperature phases could shed some light on the behaviour of the EPR spectra in the intermediate phase. In this phase, analysis of the EPR line features was achieved using a static model where the EPR spectra are accounted for with the help of a limited number of discrete lines and a dynamic model adapted from motion narrowing theory [7]. It seems that static disorder is present in the material in the wide temperature range of the intermediate phase and a departure from this scheme is manifested 20 K below T_0 where the disorder became dynamic like. Knowledge of the SHPs permits us to identify the microscopic origin of the disorder as arising from different compressions of the [Mn(H$_2$O)$_6$]$^{2+}$ octahedra along their [111] direction.

2. Preliminary presentation of electron paramagnetic resonance investigations

Mn^{2+} ($S = \frac{5}{2}$; $I = \frac{5}{2}$) paramagnetic probes are substituted for Mg^{2+} ions inside six water molecule cages. This substitution in a weak concentration is assumed to be neutral so that the information inferred from these probes mirrors the intrinsic structural change at the Mg^{2+} sites. The phenomenological spin Hamiltonian used for the interpretation of EPR spectra is used in the following form:

$$\mathcal{H} = \beta H \cdot \tilde{g} \cdot S + \frac{1}{3} \sum_{m=-2}^{m=2} b_2^m O_2^m + \frac{1}{60} \sum_{m=-4}^{m=4} b_4^m O_4^m + S \cdot \tilde{A} \cdot I \qquad (1)$$

where $\tilde{g}$ and $\tilde{A}$ are the Landé and hyperfine tensors, respectively, O_n^m are the standard Stevens spin operators and the sums represent the crystal-field contributions. S and I are the Mn^{2+} electronic and nuclear spins, respectively, and $\mathcal{H}$ must be invariant by the symmetry operations of the paramagnetic probe host site.

The magnetic axes Z and X for a $[Mn(H_2O)_6]^{2+}$ complex are chosen to be along the [101] and the [010] directions, respectively, of the monoclinic unit cell (figure 1). The Z direction coincides also, above T_c, with the [111] axis of the Mn^{2+}-centred octahedra. The symmetry of the metal site is C_{3i} in the high-temperature phase or in the intermediate phase and it is supposed to be C_{2h} in the monoclinic phase [1]. We outline below the procedure used for the determination of the SHPs.
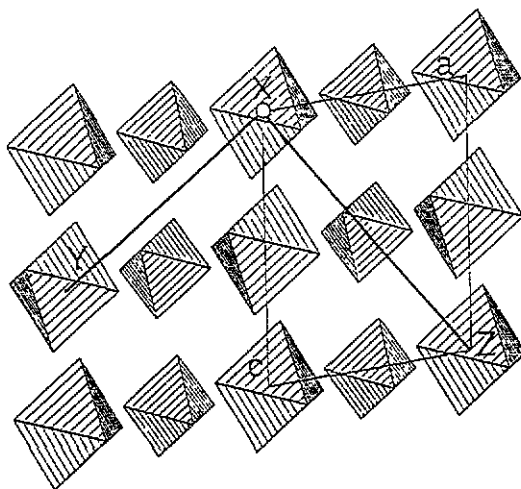

Figure 1. Projection of the $MgSiF_6 \cdot 6H_2O$ structure looking down the [010] axis of the monoclinic unit cell. The complexes $[SiF_6]^{2-}$ and $[Mg(H_2O)_6]^{2+}$ are represented by the small and large octahedra, respectively. Also shown are the location of the magnetic axes of $[Mn(H_2O)_6]^{2+}$ with respect to the crystal axes.

First, we measure the fine-structure resonance positions for different orientations of the external magnetic field H. However, because of overlapping of the hyperfine lines, it was impossible to perform measurements in some H orientations. The resonance positions associated with different electronic transitions are calculated using the above spin Hamiltonian (1) without the hyperfine term. Working on the $|M_S\rangle$ basis, i.e. on a 6×6

matrix, we were able to determine with good accuracy the fine-structure parameters, i.e. the b_n^m-values and the $\tilde{g}$-tensor components.

In a second step, we introduce the hyperfine interaction and the hyperfine line positions are calculated by diagonalizing the Hamiltonian (1) on the $|M_S, m_I\rangle$ basis, i.e. on a 36×36 matrix. These calculated resonance positions are used with suitable linewidths and lineshapes to fit the experimental spectra. To check the validity of the determined set of SHPs, we also fitted the experimental spectra for the magnetic field orientations where overlapping occurs. Then, we determined very accurately the fine-structure terms and the hyperfine parameters.

3. Spin-Hamiltonian parameters in the rhombohedral phase

The EPR experiments were performed on Bruker EPR spectrometer working at 10 GHz (X band). The samples used have the dimensions 3 mm × 1 mm × 1 mm with a cleaved plane perpendicular to the monoclinic [010] direction. The ratio of substitutional paramagnetic impurity concentrations in the sample was $[Mn^{2+}]/[Mg^{2+}] \simeq 0.01$. The Mn^{2+} EPR spectra are recorded for various orientations of the applied magnetic field H at $T = 370$ K. Only one magnetic site was observed and the simplest EPR spectrum, obtained for H along the magnetic axis Z, consists of five electronic transitions; each of these is split into six lines owing to the hyperfine interaction. For this orientation a maximum spread was obtained and we did not observe any forbidden hyperfine lines in the central sextuplet $|M_S, m_I\rangle = |\frac{1}{2}, m_I\rangle \leftrightarrow |-\frac{1}{2}, m_I\rangle$ (figure 2(a)). This demonstrates that the crystal-field interaction is axial along the [111] direction of the $[Mn(H_2O)_6]^{2+}$ octahedra which is also the direction of the pseudo-hexagonal C_h axis.

The spectra in this phase are well described with the spin Hamiltonian in the form

$$\mathcal{H} = \beta H \cdot g \cdot S + \tfrac{1}{3} b_2^0 O_2^0 + \tfrac{1}{60}(b_4^0 O_4^0 + b_4^3 O_4^3) + S \cdot A \cdot I$$

with the following values of the parameters: $b_2^0 = (281 \pm 2) \times 10^{-4}$ cm^{-1}, $b_4^0 = (2.7 \pm 0.5) \times 10^{-4}$ cm^{-1} and $b_4^3 \simeq 0$ cm^{-1}; $g_x = g_y = 2.007 \pm 0.002$ and $g_z = 1.996 \pm 0.002$; $A_x = A_y = (-90.9 \pm 0.2) \times 10^{-4}$ cm^{-1} and $A_z = (-89.4 \pm 0.2) \times 10^{-4}$ cm^{-1}. It seems that the dominant crystal-field contribution is due to the parameter b_2^0. This indicates, following the absolute sign of b_2^0, a compression or an elongation of the magnetic complexes along their [111] direction.

4. Spin-Hamiltonian parameters in the low-temperature phase

The EPR studies were performed at 250 K, sufficiently far from the transition temperature T_c. In this phase the sample is twinned and contains three twin components [2, 3]. They are related to each other by a rotation of 120° about the monoclinic [101] axis.

By EPR we were able to observe six inequivalent magnetic sites for general orientations of the external magnetic field H. Only three inequivalent sites are present for H rotating in the (010) plane and all the sites are equivalent for H oriented along the [101] monoclinic direction. These observations are consistent with the crystallographic studies [8]; the unit cell contains two equivalent $[Mg(H_2O)_6]^{2+}$ complexes with respect to a glide plane orthogonal to the [010] direction.
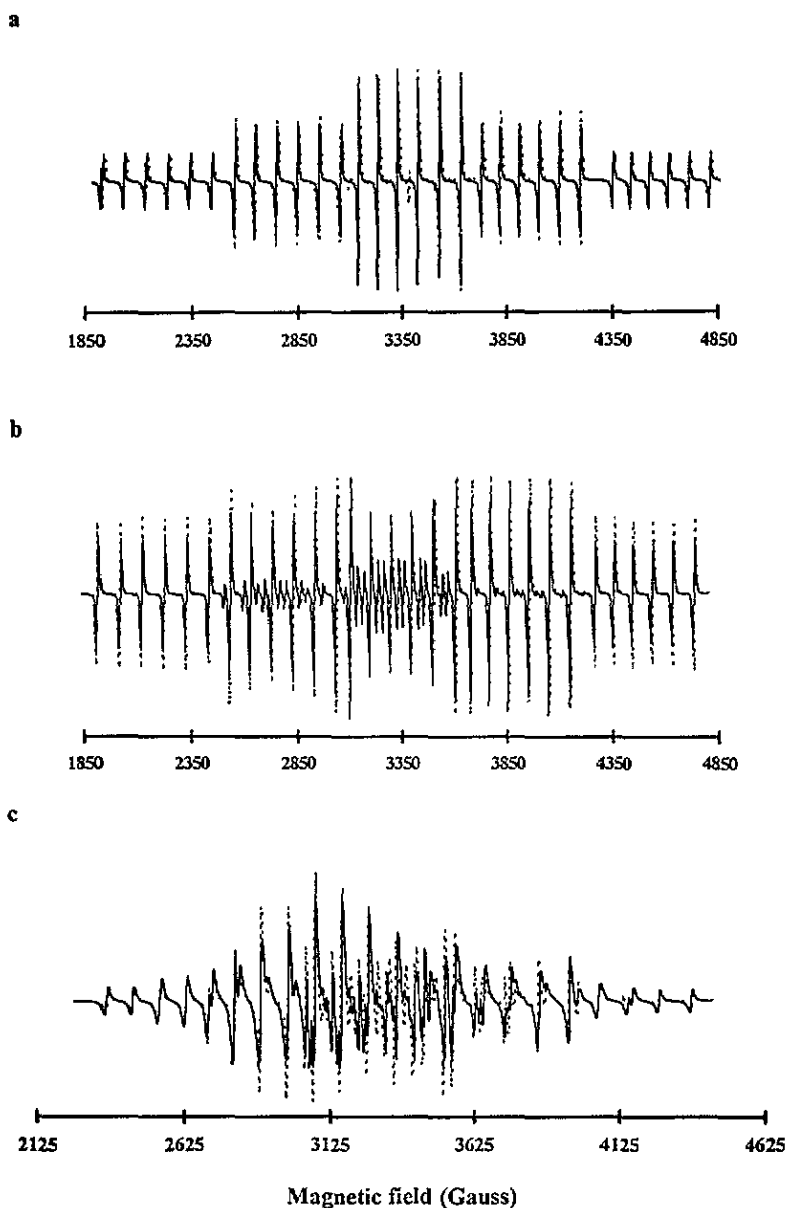
a

1850   2350   2850   3350   3850   4350   4850

b

1850   2350   2850   3350   3850   4350   4850

c

2125   2625   3125   3625   4125   4625

Magnetic field (Gauss)

Figure 2. Experimental (———) and calculated (· · · · · ·) EPR spectra of a Mn^{2+} ion in the rhombohedral and monoclinic phases of $MgSiF_6 \cdot 6H_2O$: (a) rhombohedral phase, H parallel to the [111] direction of the $[Mg(H_2O)_6]^{2+}$ octahedron; (b) monoclinic phase, H parallel to the [101] monoclinic direction; (c) monoclonic phase, H perpendicular to the [101] direction.

With the C_{2h} local symmetry of the metal site in this phase, the appropriate spin Hamiltonian is of the following form:

$$\mathcal{H} = \beta H \cdot \tilde{g} \cdot S + \frac{1}{3} \sum_{m=-2}^{m=2} b_2^m O_2^m + \frac{1}{60} b_4^0 O_4^0 + S \cdot \tilde{A} \cdot I.$$

Some terms permitted by symmetry are not included in the above expression because of their insignificant values.

We have used the procedure described in section 1 for the simulations of the experimental EPR spectra recorded at different orientations of the applied magnetic field. Some examples of the experimental and reconstructed spectra are shown in figures 2(b) and 2(c). The EPR results deduced from these simulations are summarized as follows: $b_2^0 = (275 \pm 3) \times 10^{-4}$ cm^{-1}, $b_2^1 = (-216 \pm 3) \times 10^{-4}$ cm^{-1}, $b_2^{-1} = (-24 \pm 4) \times 10^{-4}$ cm^{-1}, $b_2^2 = (-98 \pm 4) \times 10^{-4}$ cm^{-1}, $b_2^{-2} = (-51 \pm 4) \times 10^{-4}$ cm^{-1} and $b_4^0 = (2.8 \pm 0.4) \times 10^{-4}$ cm^{-1}. The components of the Landé $\tilde{g}$-tensor and the hyperfine $\tilde{A}$-tensor are isotropic within experimental accuracy: $g_x = g_y = g_z = 2.000 \pm 0.002$; $A_x = A_y = A_z = (-91 \pm 0.2) \times 10^{-4}$ cm^{-1}.

This set of the SHPs corresponds to a paramagnetic site (labelled ITC1) in one twin component with the choice of the magnetic framework R_{mf} axes Z and X, respectively, along the monoclinic [101] and [010] directions.

The second paramagnetic site in the same unit cell (labelled IITC1) is equivalent to ITC1 with respect to the glide plane (010) and possesses the same set of SHPs except for the sign of b_2^1 and b_2^{-2}. For the second crystal twin component, the paramagnetic sites labelled ITC2 and IITC2 have the same sets of parameters as above. Their magnetic framework are deduced from that of ITC1 or IITC1 by a rotation of 120° around the [101] direction. The same conclusion holds for the third twin component (ITC3 and IITC3 magnetic sites). Their magnetic framework are deduced from those of ITC1 or IITC1 by rotation of 240° around the [101] monoclinic direction. From these results, we can determine the direction of the principal magnetic framework R_{pmf} axes (X_{m}, Y_{m} and Z_{m}) for one magnetic site in a given crystal twin component (figure 3). Suitable rotations of the magnetic axes permit us to reduce the quadrupolar SHPs to the following contributions: $b_2^0 = (278 \pm 3) \times 10^{-4}$ cm^{-1}, $b_2^2 = (-117 \pm 4) \times 10^{-4}$ cm^{-1}, $b_4^0 = (2.6 \pm 0.5) \times 10^{-4}$ cm^{-1} and $b_4^0 = (6.3 \pm 0.5) \times 10^{-4}$ cm^{-1}.

We have reported in figure 3 the different steps for the transformation of R_{mf} into R_{pmf}. The b_2^2-value indicates a distortion of the complexes [Mg(H$_2$O)$_6$]$^{2+}$ in the plane perpendicular to the [101] direction.

5. Interpretation of the spin-Hamiltonian parameters in the monoclinic and the rhombohedral phases

In order to interpret the zero-field splitting in this material, we used the superposition model (SM) widely applied to account for the SHPs of d^5 ion ground states [9–11]. In this framework, a given quadrupolar SHP b_2^m can be expressed in the following form:

$$b_2^m = \sum_i \bar{b}_2(r_i) K_2^m(\theta_i, \varphi_i)$$

where r_i, θ_i and φ_i represent the length, the azimuthal angle and the polar angle, respectively, of the ligand(i)–paramagnetic ion bond, with respect to the magnetic framework in which the SHPs are determined. The functions $K_2^m(\theta_i, \varphi_i)$ are tabulated in [10] and $\bar{b}_2(r_i)$ varies as a power-law expression [10]:

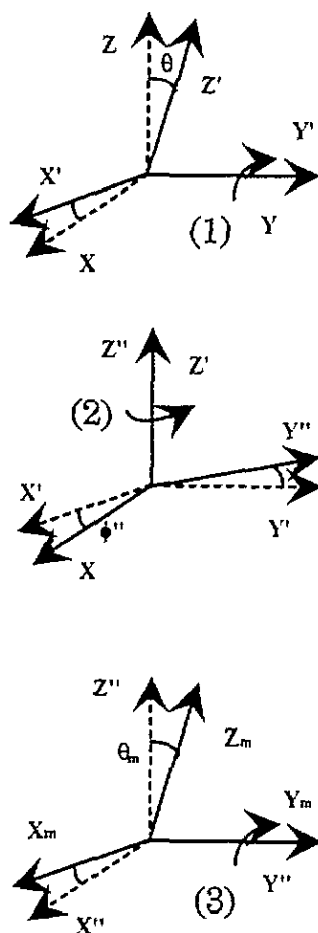$$\bar{b}_2(r_i) = \bar{b}_2 \left(\frac{R_0}{r_i} \right)^t$$

Figure 3. Successive rotation transformations of the magnetic framework R_{mf} (X, Y, Z) into the principal magnetic framework R_{pmf} (X_m, Y_m, Z_m): (1) $\theta = -4.9°$, (2) $\phi = 14°$; (3) $\theta_m = -1.9°$.

where $\bar{b}_2$ is an intrinsic parameter, R_0 represents an average distance for the metal–ligand pair and for the coordination number under consideration and t is a characteristic exponent which depends on the ligand species and the paramagnetic ion.

We have used the crystallographic data of [8] for the monoclinic low-temperature phase and that recently reported [12] for the rhombohedral phase of $MgSiF_6 \cdot 6D_2O$. The magnetic framework used is defined in figure 1 and the sets $(r_i, \theta_i, \varphi_i)$ are summarized in tables 1 and 2 for the two phases.

The experimental SHPs in the monoclinic and rhombohedral phases were accounted for using the above-mentioned model for the octahedron $[Mn(H_2O)_6]^{2+}$. Angular and bond length relaxations (tables 1 and 2) were allowed, owing to the substitution of Mg^{2+} by a cation of larger size. According to previous results [13] on Mn^{2+} ions in other host lattices, the exponent t was taken equal to 7. The calculated SHPs are compared with the experimental values in table 3. We found that $\bar{b}_2(R_0) = 1640 \times 10^{-4}$ cm^{-1} for $R_0 = 2.059$ Å, i.e. the ligand–paramagnetic ion distance in the rhombohedral phase. For the average distance of

Table 1. Coordinates $(r_i, \theta_i, \varphi_i)$ related to the ith bond in a $[Mn(H_2O)_6]^{2+}$ octahedron with respect to the magnetic framework R_{mf} in the monoclinic phase.

θ_i	$\delta\theta_i$	φ_i	$\delta\varphi_i$	r_i	δr_i
54.86	−0.5	−136.25	0.5	2.115	−0.014
125.14	0.5	43.75	0.5	2.115	−0.014
55.23	−0.5	−17.73	−1.3	2.107	0
124.77	0.5	162.27	−1.3	2.107	0
52.77	−1.3	102.05	0.9	2.083	0.015
127.22	1.3	−77.95	0.9	2.083	0.015

Table 2. Coordinates $(r_i, \theta_i, \varphi_i)$ related to the ith bond in a $[Mn(H_2O)_6]^{2+}$ octahedron with respect to the magnetic framework R_{mf} in the rhombohedral phase.

θ_i	$\delta\theta_i$	φ_i	$\delta\varphi_i$	r_i	δr_i
53.98	−0.395	−17.44	0	2.060	0
126.02	0.395	162.56	0	2.060	0
53.98	−0.395	−137.45	0	2.060	0
126.02	0.395	42.55	0	2.060	0
53.98	−0.395	102.55	0	2.060	0
126.02	0.395	−77.45	0	2.060	0

Table 3. Comparison between the experimental spin-Hamiltonian parameters and the calculated values using the superposition model.

Experimental SHP	SM model
$b_2^0 = 272$	263
$b_2^1 = -216$	−222
$b_2^2 = -98$	−107
$b_2^{-1} = -24$	−22
$b_2^{-2} = -51$	−53
b_2^0 (high-temperature phase) $= 281$	281

2.101 Å in the monoclinic phase, we found that $\bar{b}_2(2.101 \text{ Å}) = 1421 \times 10^{-4} \text{ cm}^{-1}$. This value is of the same order of magnitude as but of opposite sign to that determined in the cases of Mn^{2+} ion in MgO [13].

The absolute signs of our SHPs are correctly checked using the hyperfine splitting and the intensity of the forbidden hyperfine lines. Indeed, when the magnetic field H is oriented along the principal magnetic axis Z, the spectrum exhibits a maximum spread (figure 2(b)). A given electronic transition is split by the hyperfine interaction; this gives rise to permitted and forbidden hyperfine lines. The permitted hyperfine lines are not equidistant and the experimental positions are correctly accounted for using a positive sign for b_2^0 and negative signs for the other parameters. This choice of the signs reproduces also the observed intensity of the forbidden hyperfine lines. Such arguments work in the case of a negative sign for the hyperfine constants; this is the case for Mn^{2+} ions in many host lattices [14]. We may conclude that, in the case of a Mn^{2+} ion surrounded by water molecules in an octahedral arrangement, the intrinsic parameter $\bar{b}_2$ is positive.

On the other hand, we have not applied the SM to the fourth-rank parameters b_4^m because of the weak value of the single parameter found here, namely $b_4^0 = (2.8 \pm 0.5) \times 10^{-4} \text{ cm}^{-1}$.

The SM gives quite satisfactory results for the Mn^{2+} SHP in this fluorosilicate system.

However, reasonable local relaxations are necessary and the differences between the SHPs in the rhombohedral and monoclinic phases are the consequence of the ligand coordinate variations as reported in tables 1 and 2.

In the rhombohedral phase, the positive sign of the quadrupolar crystal-field parameter b_2^0 indicates a compression of the [Mn(H$_2$O)$_6$] octahedron along the pseudo-hexagonal axis C_h.

In the monoclinic phase, a compression of the Mn^{2+}-centred octahedron, a variation in the Mn–H$_2$O bond lengths as well as different bond rotations around the C_h axis lead to the experimental set of SHPs.

6. Electron paramagnetic resonance study of the intermediate phase

6.1. Experimental results

In this phase, we have examined the thermal evolution of some EPR spectra for particular orientations of the applied magnetic field H.

For H oriented along the pseudo-hexagonal C_h axis, we have analysed the behaviour of the spectra associated with the transitions A ($|M_S, m_I\rangle = |-\frac{5}{2}, -\frac{5}{2}\rangle \leftrightarrow |-\frac{3}{2}, -\frac{5}{2}\rangle$) and B ($|\frac{5}{2}, \frac{5}{2}\rangle \leftrightarrow |\frac{3}{2}, \frac{5}{2}\rangle$) between T_0 and T_c; A and B are located at high- and low-magnetic-field positions, respectively. Figure 4 shows the thermal evolution of the EPR A spectrum. We may note that, below $T_c = 301$ K, each transition A emanating from the three twin components of the sample merges into a single line. On heating the sample above T_c, an abrupt decrease in the line intensity is observed whereas two other lines begin to develop at different magnetic field positions. The resulting spectrum contains two components: a sharp line and a broad line which exhibits better narrowing on heating the sample.

For H oriented along the C_h axis, we have also examined the behaviour of the central line CL, namely $|M_S, m_I\rangle = |\frac{1}{2}, m_I\rangle \leftrightarrow |-\frac{1}{2}, m_I\rangle$. The important change in this spectrum consists of the sudden disappearance of the forbidden hyperfine lines at the transition temperature. This indicates unambiguously the existence of reorientations of the [Mn(H$_2$O)$_6$]$^{2+}$ complexes on passing the phase transition at T_c.

Finally, for the rotation of H in the plane perpendicular to the C_h axis, the EPR spectra do not exhibit any anisotropy. The evolution of the EPR spectrum associated with the transition C ($|M_S, m_I\rangle - |\frac{5}{2}, \frac{5}{2}\rangle \leftrightarrow |\frac{3}{2}, \frac{5}{2}\rangle$) was also studied in the intermediate phase and comparison is made with the behaviours of the A and B transitions for H oriented along the C_h axis.

6.2. Discussion

As long as we assume that the essential crystal-field contributions come from the nearest neighbours of the paramagnetic ion (section 4), the following conclusions can be drawn.

First, the temperature behaviour of the EPR spectra for H parallel to the C_h axis indicates that the [Mn(H$_2$O)$_6$]$^{2+}$ octahedra undergo rotation at T_c. The direction of their magnetic axes Z_m change and became parallel to the C_h axis. The low-temperature SHP $b_2^{\pm 1}$ vanishes above T_c.

Second, the EPR spectra above T_c are found to be invariant with respect to the H rotations about the C_h axis and this means that no distortion of the Mn–H$_2$O bonds exists in this plane. As a consequence, the low-temperature parameters $b_2^{\pm 2}$ in the spin Hamiltonian could be neglected. The crystal field above T_c is purely axial and can be characterized by the parameter b_2^0. The appearance of at least two EPR lines for each transition above T_c
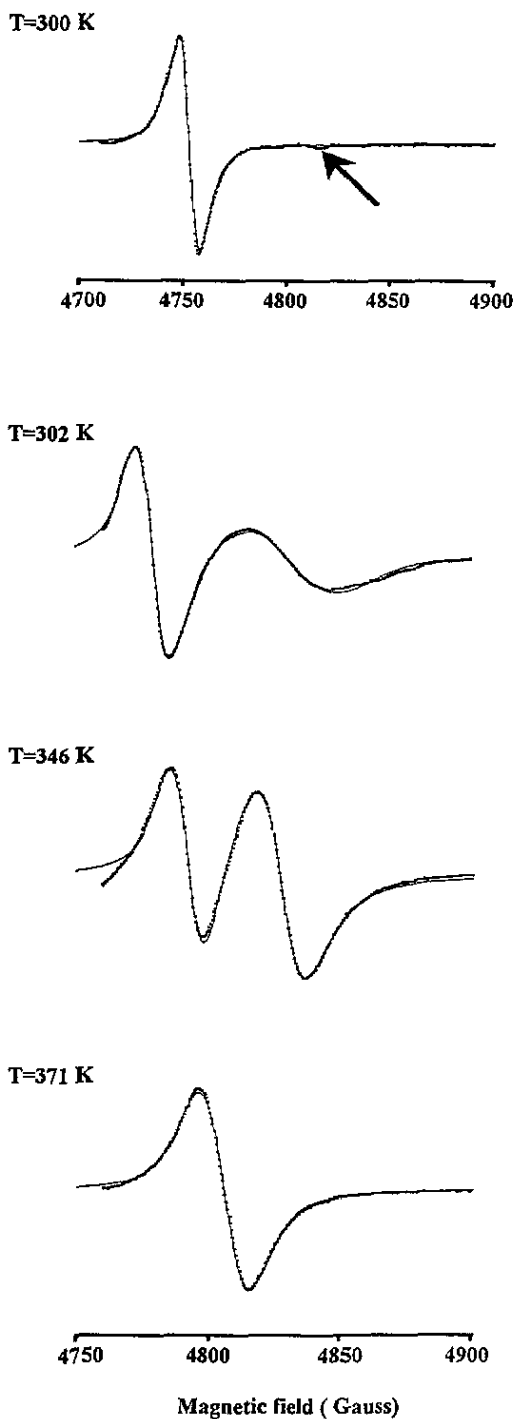
Figure 4. Thermal evolution of EPR spectra related to the transition A $(|M_S, m_I\rangle = |-\frac{5}{2}, -\frac{5}{2}\rangle \leftrightarrow |-\frac{3}{2}, -\frac{5}{2}\rangle)$ in the intermediate phase of $MgSiF_6 \cdot 6H_2O$. A single line below $T_c = 301$ K gives rise above T_c to a narrow line L_n and a broad line L_b which show better resolution on heating the sample. The arrow on the first spectrum indicates the embryo of the lines L_n and L_b which develop above T_c.

indicates the existence of two magnetic sites of local symmetry C_{3i} which are associated with different values of b_2^0. We may note that the analysis of section 4 yields a difference in b_2^0 of about 10×10^{-4} cm^{-1} through the variation in the azimuthal bond angles in a $[Mn(H_2O)_6]^{2+}$ complex by only $0.05°$.

In the intermediate phase, the EPR line features were analysed using two approaches, namely the static model and the order–disorder model.

In the former the EPR spectra A, B and C were fitted using a set of two discrete lines. The splitting ΔH for H along the C_h axis was found to be twice that in the perpendicular direction and decreases on going from T_c to T_0. This is consistent with the temperature variation in b_2^0 only. However, the variation in b_2^0 compatible with a local symmetry C_{3i} can be realized only through a compression or an elongation of the $[Mn(H_2O)_6]^{2+}$ octahedra along the C_h axis. On the other hand, if reorientations of $[Mn(H_2O)_6]^{2+}$ octahedra exist above T_c, we may conclude, from the EPR results, that the reorientations would be around the C_h axis, and then no distortion could be generated from these motions. So we think that the distortions of these octahedra could result from the motion of the water molecules. In particular, it is well known that reorientations of the $[SiF_6]^{2+}$ octahedra exist and the observed variation in b_2^0 might be the consequence of the change in O–H$\cdots$F hydrogen bonds which affects the magnetic sites.

From this static analysis, we have found two magnetic sites which differ in their parameters b_2^0. Their populations could be obtained from the integrated EPR signal. This situation, valid for temperatures lower than $T_{c1} = T_0 - 22$ K, could be connected with the existence of two different domains with size ratio reported in figure 5(a) at different temperatures. From the crystallographic analysis of [2] realized above T_c, it was found that the structure is formed by two domains with nearly the same occupation rates in agreement with our EPR results in the vicinity of T_c. Above T_{c1}, we have to take into account the existence of a third magnetic site. Its spectral intensity increases just above T_{c1} followed by a decrease on going towards T_0. Thus we can assume that another domain begins to develop to the detriment of the sizable domain realized below T_{c1}. The only merit of this static model for the EPR line analysis it that it yields information about the dominant magnetic site populations. In particular above T_{c1}, we cannot say how the appearance or disappearance of different kinds of magnetic site is realized in such a system.

Therefore, a second approach was developed to see whether dynamic disorder in the material leads to the observed spectral features. Disorder could be generated, when the temperature increases towards T_0, by the reorientation of the water molecules, leading to different configurations of the magnetic complexes because of the variation in the O–H$\cdots$F bonds, and also by those magnetic probes which are located near the domain boundaries.

We used a simple dynamic model, adapted from motion narrowing theory [7], for the EPR line feature analysis. Following the above-mentioned theory, the intensity of spectral lines at a given magnetic field H is of the form

$$I(H) = \text{Re}(W A^{-1} \cdot 1) \tag{2}$$

where W is a vector with components W_α giving the population of the magnetic sites in the α configuration. A^{-1} is the inverse of a square matrix with order equal to the number of different magnetic complex configurations. A depends on the resonance fields and on the frequency jumps between different configurations. 1 represents a vector with all components equal to 1.

As we described above using the static model, we assumed the existence of three kinds of magnetic site which differ in their parameters b_2^0 (figure 5(b)). The configuration denoted
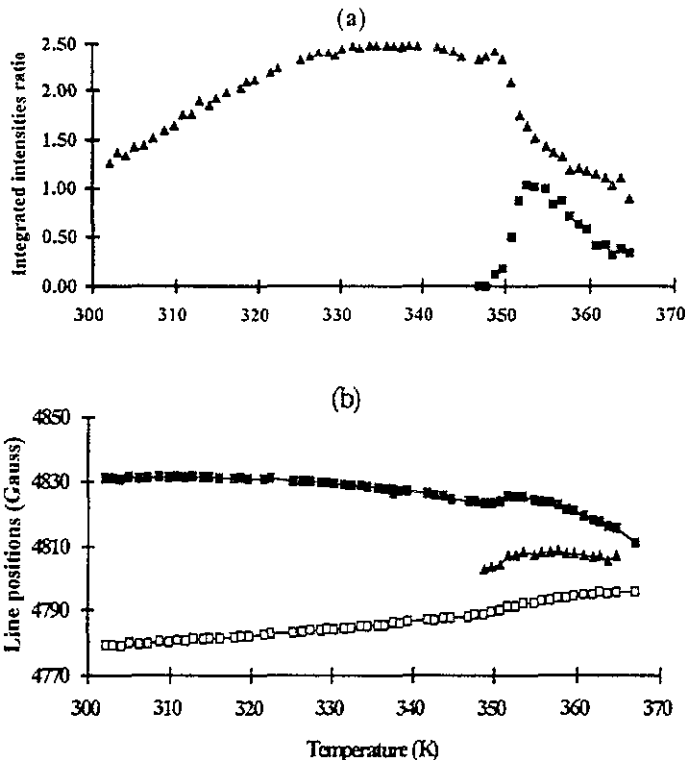
Figure 5. Results of the static analysis of the EPR spectrum in the intermediate phase. Below $T_{c1} = 348$ K, only two discrete lines L_n and L_b are used to reproduce the spectrum related to the A transition (see text). Above T_{c1}, a third line L_3 is necessary to improve the fit. (a) Integrated intensities ratio: ▲, $I(L_b)/I(L_n)$; ■, $I(L_3)/I(L_n)$. (b) Resonance positions of the lines L_n (—□—), L_b (—■—) and L_3 (—▲—) associated with the low (b_2^0)-value, the high $(b_2^0)_+$-value and the intermediate $(b_2^0)_0$-value, respectively.

(+) is associated with the magnetic site with the highest b_2^0-value, the second denoted (−) is associated with the lowest b_2^0-value and the third denoted (0) is associated with an intermediate b_2^0-value. The dynamic process could be introduced by considering jumps between the different configurations as illustrated in figure 6. The frequency jumps ν_{ij} ($i, j = +, 0, -$) are adjustable parameters and a computer program was developed to fit the experimental spectra using this dynamic model between T_{c1} and T_0. We can deduce the populations (figure 7) and the frequency jumps (figure 8) between these configurations.

The populations W_+ and W_- are found to be nearly equivalent and exhibit a slight increase on approaching T_0. The magnetic complexes in the configuration (0) have a rate occupation in the crystal about 15% at T_{c1} and decrease on going towards T_0. The intermediate configuration (0) disappears in the vicinity of T_0 and at the same time the EPR spectrum merges into a single line because of the increase in the frequency jumps between the configurations (+) and (−). We may note that, on approaching T_0, the EPR spectra could be fitted by considering only two configurations, namely (+) and (−). The frequency jumps (figure 8) permit us to determine the relaxation times involved in the dynamic process. Indeed, the rates of change in the ith configuration population are given by the following master equation [7]:
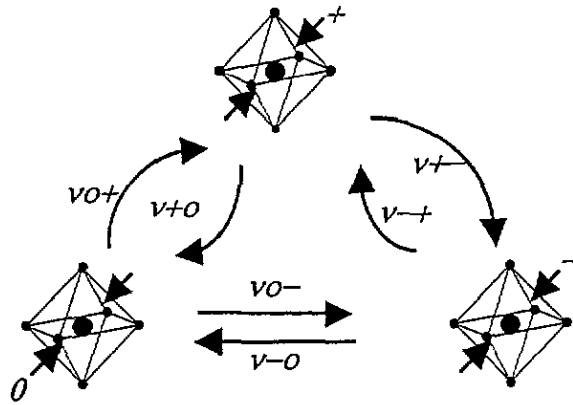
Figure 6. A schematic representation of the $[Mn(H_2O)]^{2+}$ octahedra ($\bullet$, Mn^{2+}; $\bullet$; H_2O) with different compressions shown by arrows along the [111] octahedron direction. Also depicted are the frequency jumps (ν_{ij}, $i, j = +, 0, -$) between the different configurations of the magnetic complexes.
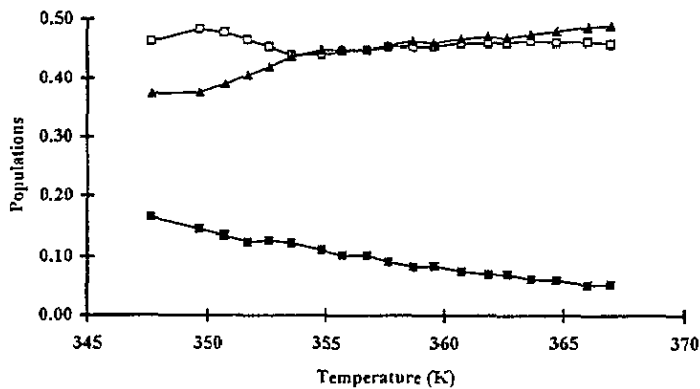

Figure 7. Populations of the magnetic complex configurations inferred from the reconstruction of the EPR spectra using the dynamic model: —□—, W_+; —▲—, W_-; —■—, W_0.

$$\frac{dN_i}{dt} = -N_i \sum_{j \neq i} \nu_{ij} + \sum_{j \neq i} N_j \nu_{ji} \qquad (i, j = +, 0, -) \tag{3}$$

with N_i, close to W_i on a characteristic time scale of the EPR technique of the order of 10^{-8} s.

The resolution of a differential system of three equations of type (3) at different temperatures yields two relaxation times τ_1 and τ_2 reported in figure 9. We may note that, when the temperature decreases from T_0, τ_1 is found to follow an Arrhenius-like behaviour with an activation energy of about 1320 K and an amplitude of the order of 0.13×10^{-9} s. τ_2, on the contrary, exhibits a smooth decrease, reaches a minimum at around $T_{c1} + 5$ K and increases towards T_c. This unusual thermal evolution of τ_2 cannot be explained in the framework of local configurations, and structural information in this temperature range is needed to understand such behaviour. However, the increases in τ_1 and τ_2 on approaching
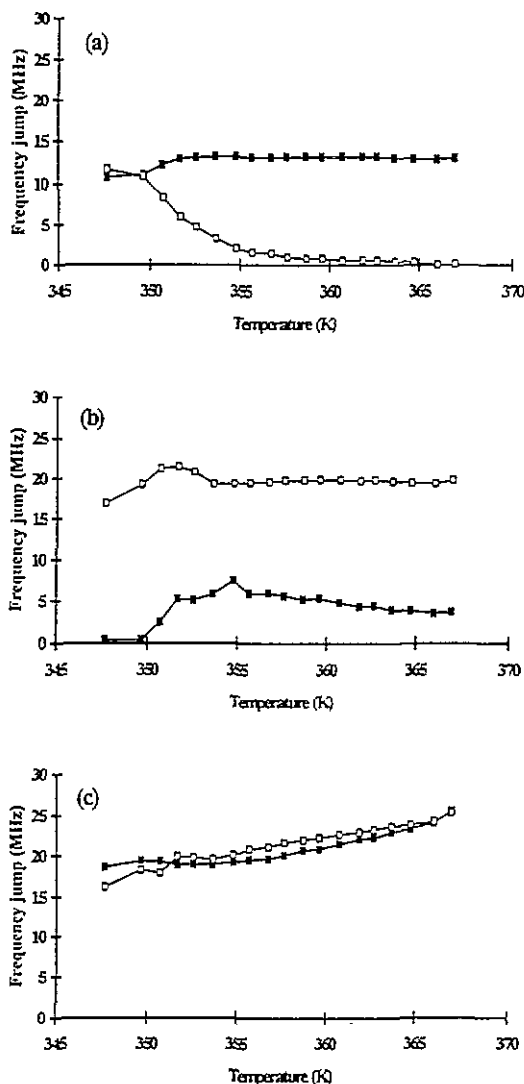
Figure 8. Frequency jumps between the different configurations considered in the dynamic model. (a) Between the configurations (+) and (0): □, ν_{+0}; ■, ν_{0+}. (b) Between the configurations (−) and (0): □, ν_{0-}; ■, ν_{-0}. (c) Between the configurations (+) and (−): □, ν_{+-}; ■, ν_{-+}.

T_{c1} indicate a slowing down of the dynamic process below T_{c1} in concordance with the static analysis of the EPR spectra.

It is worth noting that, near T_0, the relaxation of the (+) and (−) configurations is essentially dominated by τ_1 whereas the relaxation of the intermediate configuration is governed by τ_1 and τ_2. The decrease in τ_1, the increase in the frequency jumps ν_{+-} and ν_{-+} and the disappearance of the intermediate configuration suggest a disordered phase above T_0 with two configurations (+, −) of the metal-centred octahedra. Below T_{c1}, the dynamic model cannot account for the observed EPR spectral features. The reconstruction of the spectra needs unambiguously only two discrete lines. This is valid for different samples
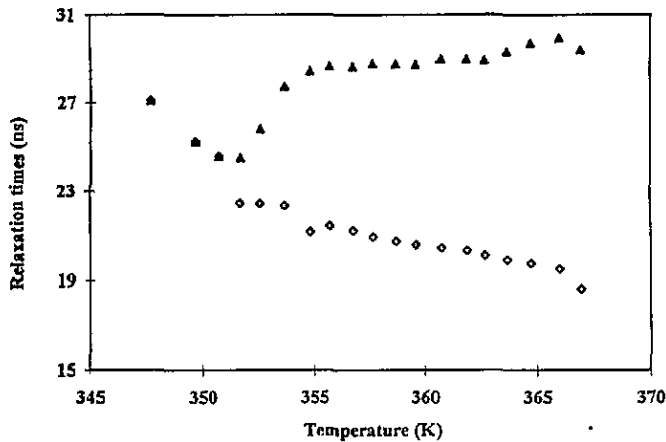
Figure 9. Relaxation times involved in the dynamic process: —☐—, τ_1; —▲—, τ_2.

studied as well as for deuterated samples. Static disorder which generates two magnetic sites is a plausible explanation in this temperature range. The paramagnetic probe environments differ only in their compression along the C_h axis.

7. Conclusions

The characterization of the crystal-field interaction is made accurately in the different phases of $MgSiF_6 \cdot 6H_2O$. The SHPs are interpreted with respect to the crystalline environment of the magnetic probes.

In the intermediate phase, two different procedures, namely static and order–disorder, were used to describe the experimental spectra of Mn^{2+}. Both of the methods used have given quite satisfactory results in well defined temperature regions and enables us to reconstruct the observed spectra. It seems that the crystal exhibits static disorder below T_{c1} and dynamic disorder with low frequencies above T_{c1}. The crystalline phase above T_0 is disordered and contains two configurations of the metal-centred octahedra. The origin of the disorder lies in different compressions of the octahedra $[Mg(H_2O)_6]^{2+}$ along their [111] direction.

Acknowledgments

References

[1]   Price D C 1987 *Can. J. Phys.* **65** 1280
[2]   Chevrier G and Jehanno G 1979 *Acta Crystallogr.* A **35** 912
[3]   Hrabanski R, Sczaniecki P B and Stankowski J 1979 *Phys. Status Solidi* a **51** 243
[4]   Ziatdinov A M, Kuryavii W G and Davidovich A L 1985 *Fiz. Tverd. Tela* **27** 2152; 1987 *Fiz. Tverd. Tela* **29** 215

[5]   Hrabanski R 1991 *Ferroelectrics* **124** 333 and references therein
[6]   Blinc R 1981 *Phys. Rep.* **79** 331
[7]   Abragam A 1961 *Principles of Nuclear Magnetism* (Oxford: Clarendon) ch X
[8]   Syoyoma S and Osaki K 1972 *Acta Crystallogr.* B **28** 2626
[9]   Newman D J and Urban W 1972 *J. Phys. C: Solid State Phys.* **5** 3101
[10]   Newman D J and Betty N G 1989 *Rep. Prog. Phys.* **52** 699
[11]   Moreno M 1990 *J. Phys. Chem. Solids* **51** 835
[12]   Chevrier G 1992 *J. Solid State Chem.* **99** 276
[13]   Siegel E and Muller K A 1979 *Phys. Rev.* B **19** 109 and references therein
[14]   Rousseau J J, Leble A and Fayet J C 1978 *J. Physique* **39** 1215